Soft Matter

PAPER

View Article Online
View Journal | View Issue

Cite this: *Soft Matter*, 2016, 12, 7186

Let's twist again: elasto-capillary assembly of parallel ribbons†

Antoine Legrain,*[ab] Erwin J. W. Berenschot,[a] Leon Abelmann,[ac] José Bico*[d] and Niels R. Tas[a]

Received 17th April 2016,
Accepted 3rd August 2016

DOI: 10.1039/c6sm00910g

www.rsc.org/softmatter

We show the self-assembly through twisting and bending of side by side ribbons under the action of capillary forces. Micro-ribbons made of silicon nitride are batch assembled at the wafer scale. We study their assembly as a function of their dimensions and separating distance. Model experiments are carried out at the macroscopic scale where the tension in ribbons can easily be tuned. The process is modeled considering the competition between capillary, elastic and tension forces. Theory shows a good agreement for macroscale assemblies, while the accuracy is within 30% at the micrometer scale. This simple self-assembly technique yields highly symmetric and controllable structures which could be used for batch fabrication of functional 3D micro-structures.

1 Introduction

Most Micro Electro-Mechanical Systems (MEMS) rely on the elastic deformation of small micro-machined parts to transduce a mechanical input into an electrical signal or *vice versa*. For instance, the fine tuning of the resonant properties of micro-cantilevers offers broad sensing capabilities in mechanics, chemistry or biology, where the detection of small mass changes with high sensitivity is required.[1] Standard micro-fabrication processes have been historically dominated by lithography.[2] However, novel techniques exploiting self-assembly through interfacial forces have emerged as powerful tools to build complex three-dimensional (3D) micro- or even nano-structures where standard top-down methods have shown limitations.[3–6]

Surface tension forces become dominant below the capillary length $L_c = \sqrt{\gamma/\rho g}$, where γ is the surface tension, ρ the density of the liquid, and g the acceleration due to gravity. At such scales, capillary forces are for instance able to deform slender microstructures typically larger than the elasto-capillary length $L_{ec} = \sqrt{B/\gamma}$, where B is the bending stiffness of the structure.[7] Such deformations have been traditionally viewed as a threat in MEMS technology, as they may lead to the disastrous stiction of flexible parts such as micro-cantilevers[8,9] or soft elastomeric structures.[10,11] Nevertheless this paradigm has progressively evolved as capillary forces may also promote the self-assembly of nanotubes or nanowire forests into complex patterns[12–14] or the folding of 2D templates into 3D origami structures.[15–21] Although the assembly of soft pillars into intriguing chiral structures has been recently reported,[22–24] most deformations involving elasto-capillary interactions rely on bending. We here investigate the spontaneous assembly of micro-ribbons into helical shapes through twisting (Fig. 1). Motivated by potential applications in micro-fabrication, we first present experiments

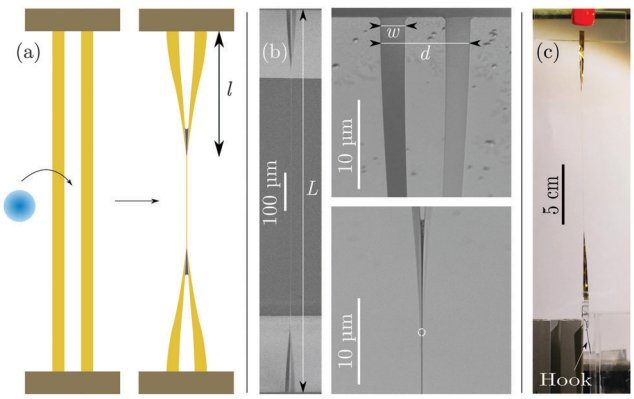

Fig. 1 (a) Elasto-capillary self-assembly involving twisting. Pairs of parallel ribbons clamped at their extremities adhere by capillary forces when put in contact with a wetting liquid. (b) SEM pictures of a millimeter-long assembled pair of silicon nitride (SiN) ribbons and close-ups on the extremities and on the adhering part, where a capillary bridge appears in dark. The assembly is symmetric and the points at which the SiN beams fully adhere and form a single thin beam are determined from SEM images (white dot on the middle bottom picture). (c) Setup for macroscopic-scale experiments. Two ribbons cut out of a thin polyester sheet are clamped at one extremity and attached but free to move up and down at the other. A hook at the bottom end is used to apply a fixed tension using calibrated weights.

[a] *MESA + Institute for Nanotechnology, University of Twente, The Netherlands*
[b] *CNRS, LTM, Grenoble, France. E-mail: antoine.legrain@cea.fr*
[c] *KIST Europe, Saarbrücken, Germany*
[d] *PMMH-ESPCI-PSL, UMR CNRS 6738, UPMC, Paris, France*

† Electronic supplementary information (ESI) available. See DOI: 10.1039/c6sm00910g

conducted at the micrometer scale. Additional model experiments at a larger scale are then described and lead to a theoretical model in the light of recent works on twisted ribbons.[25,26] This model provides a good prediction of the elasto-twist assembly at both scales and could help design a variety of twisted microstructures.

2 Elasto-capillary twisting at different scales

In this section, we first present the capillary induced self-assembly of micrometer scale ribbons obtained through lithography techniques. The microstructures are simultaneously bent, twisted, and stretched during this process. With the aim of rationalizing these different mechanisms, we then describe macroscopic scale experiments where the relevant parameters (and especially the tension) can be varied independently.

2.1 Micro-ribbons: a versatile design window

2.1.1 Fabrication. The fabrication of the micrometer sized ribbons is sketched in Fig. 2. A uniform layer of rich silicon nitride (SiN) is first deposited on a silicon wafer by low pressure chemical vapour deposition (LPCVD). Parallel stripes are next obtained through dry etching. Their length L was varied from 50 μm to 1 mm and for each length, many combinations of widths ($5 < w < 30$ μm) and separations ($15 < d < 50$ μm) were designed. An anisotropic wet etching process is then conducted: the samples are dipped in a 25 wt% tetramethylammonium hydroxide solution (TMAH) for 300 min at 95 °C. As the etching is much more efficient on silicon (Si) than on SiN, the ribbons are finally released from the substrate. Ribbons of final thickness $t = (271 \pm 10)$ nm and $t = (107 \pm 8)$ nm were fabricated from SiN layers of initial thicknesses t = 300 nm and t = 125 nm, respectively. The uncertainties in the thickness are due to the fact that the ribbons are also attacked from underneath, while thickness measurements by ellipsometry are carried out on planar, non-released parts.

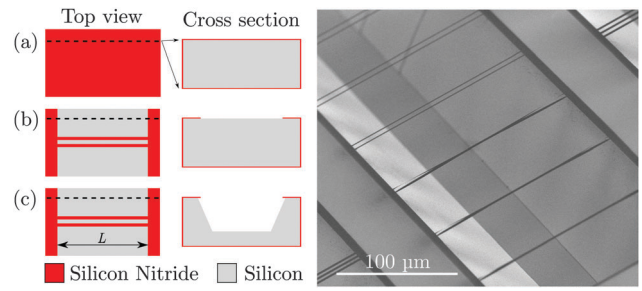

Fig. 2 Fabrication process of microscopic ribbons. (a) A conformal layer of SiN is deposited on top of a silicon wafer by low pressure chemical vapour deposition (LPCVD). (b) Patterning of SiN by dry etching. (c) Using SiN as a masking layer, silicon is etched in anisotropic wet etchant and the wires are released from the substrate. After etching the wafers are placed in water for three days. The assembly takes place after letting the wafer dry in open air. The length L, width w and spacing d of the ribbons are parameters that can be tuned on the initial mask. Right-hand side: nearly top view Scanning Electron Microscopy (SEM) picture of the resulting structures of a sample where the spacing between the ribbons is decreased. While the three pairs of ribbons with higher spacing do not adhere, the narrower ones do.

2.1.2 Measurement of the residual stress. The LPCVD process leads to residual tensile stresses in the SiN layer (our choice of rich silicon nitride instead of standard stoichiometric Si_3N_4 was actually motivated by its lower residual stress). This stress is readily estimated by measuring with a surface profilometer the slight deformation of a thin 'dummy' wafer on which a SiN layer has been deposited under the same conditions. Since both sides of the wafer get coated during the LPCVD process, one side of the wafer is stripped prior to the measurement of the stress induced curvature. Using the Stoney equation,[27] we estimated the residual stress as $\sigma_{\text{r-SiRN}} = (169 \pm 25)$ MPa. For comparison, the residual stress of stoichiometric Si_3N_4 is in the range 600 MPa to 1000 MPa.[28] The thickness of the substrates was measured using a dedicated tool (Heidenhain measuring station using a length gauge). For Young's modulus and Poisson's ratios, we used literature values of $E_{\text{SiRN}} = 290$ GPa and $\nu = 0.27$, respectively.[29]

2.1.3 Capillary self-assembly and twist. After etching, the wafers were immersed in water for three days before being removed and dried in open air in a cleanroom. This immersed period was deliberately long to let the wet etchant dilute into the large volume of water. The self-assembly takes place during drying in a time period on the order of a few minutes as can be seen in Movie 1 in ESI.† Fig. 3 shows an example of batch folding of micro-ribbons. This top view of a silicon trench (see Fig. 2) is an example of batch assembly with an increasing separation between ribbons. After the experiments, the ribbons were characterized by optical microscopy or by SEM when better magnification was necessary. The liquid was totally evaporated when pictures were taken. As a general trend, we observe that the adhesion length decreases approximately linearly as the gap between the ribbons increases. Beyond a critical gap, the ribbons cannot adhere (right-hand side in Fig. 3). These results are confirmed by a quantitative measurement of the adhesion length as a function of the separating distance for a large range of widths and lengths of the micro-ribbons as it will be discussed in section results 4.2.

2.2 Macro-ribbons: tuning the tension

2.2.1 Experimental setup. Millimeter-size ribbons were cut using a scalpel in biaxially-oriented polyethylene terephthalate (Mylar) sheets. This manual procedure provides clean cuts with no increase of thickness, in contrast with preliminary samples obtained by laser cutting. We indeed observed that the laser beam burns the material, yielding a significant increase in the thickness of the ribbon at their edges (on the order of 5 μm). The thickness t and the Young modulus E of the Mylar sheet were inferred by tensile and flexural testing (independently providing the stretching and bending stiffnesses, Et and Et^3 respectively). The tensile strength was obtained from force–displacement measurements using a dedicated machine (Instron). Flexural testing consisted in measuring the size of a racket formed by connecting the opposite ends of a strip with a droplet of wetting liquid.[7] The bending rigidity deduced from this elasto-capillary test was confirmed by monitoring the flexion

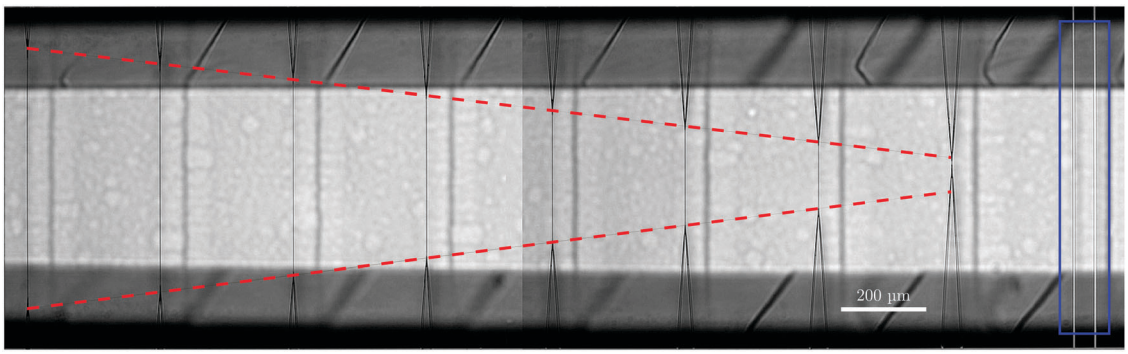

Fig. 3 Optical image of an array of pairs of ribbons after their self-assembly (L = 800 μm, w = 5 μm and t = 107 nm). The gap between the two first ribbons (left-hand side) is 5 μm and increases by 5 μm for every new pair. The red dashed lines indicate the symmetric merging of the connection points between the ribbons. The adhesion length decreases approximately linearly with the gaps separating the ribbons. In the last pair, the ribbons are too far apart to remain assembled (solid blue box).

of a strip under its own weight. We obtained $t = (13.5 \pm 14)$ μm (consistent with direct measurements through stylus profilometry) and $E_{\mathrm{mylar}} = (4.6 \pm 05)$ GPa.

2.2.2 Capillary induced twist. Macroscopic experiments were carried with the setup illustrated in Fig. 1c. Pairs of ribbons were attached vertically on both ends with a fixed separating distance (the relative distance $d/w \sim 1$ was selected to be within the same range as the microscopic scale experiments). The upper clamp is fixed while the lower attachement can move up and down. A tension was applied on the lower side by fixing weights on a hook. We used weights from 1 g to 60 g, resulting in tensile stresses in individual ribbons σ_{mylar} in the range 0.20 MPa to 20 MPa depending on the cross section of the beams. To initiate the capillary adhesion, we deposited droplets of silicone oil of surface tension $\gamma_{\mathrm{oil}} = (21.0 \pm 05)$ mN m^{-1} using a syringe. Our choice of the bridging liquid was motivated by the perfectly wetting properties of silicone oils on mylar and by its non-volatility. The contact was initially forced by bringing the top sides of the ribbons together. Nevertheless, the stability of the final assembly was probed by perturbing the ribbons with the syringe tip. Snapshots of the adhering ribbons were analyzed using the software ImageJ. The results obtained with model macroscopic experiments display the same qualitative behavior as observed at small scale: narrower ribbons display a larger contact length – *i.e.* a smaller opening length l as defined in Fig. 1(a). Note that a close-up view of the meniscus joining the ribbons shows that the contact occurs along an oblique line through the width of the ribbons (Fig. S1 in ESI†). However, the effect of this tilt in the estimation of the opening length is negligible in the limit $w \ll l$. Increasing the tensile load reduces the opening length (Fig. 4). Following these observations, we propose in the following section a quantitative model describing this elasto-capillary assembly.

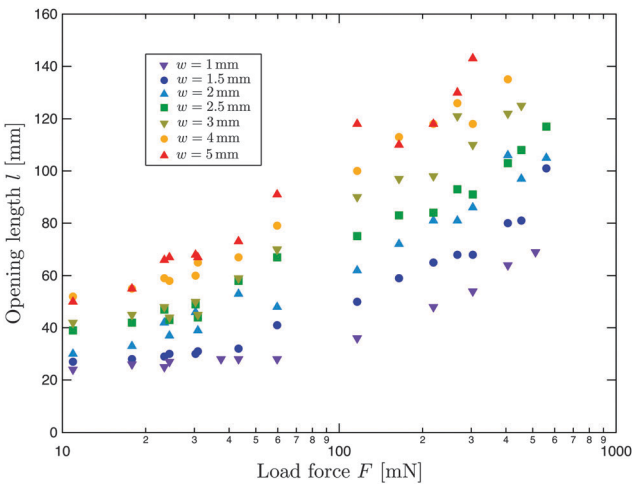

Fig. 4 Opening length l as a function of the applied load F in the case of macroscopic ribbons of increasing widths w. The total length is fixed L = 200 mm. The gap between the ribbons is null ($d = 2w$).

3 Simplified model

Based on our previous qualitative experimental observations we expect the physical ingredients involved in the problem to be interfacial forces, twisting, bending and tensile stress. In this section, we introduce a theoretical model for the capillary-induced adhesion of parallel ribbons. We first focus on the macroscopic situation and assume that the ribbons are inextensible. We then adapt this model to the case of extensible ribbons, which is relevant to our micro-scale experiments.

The parameters used for modeling are illustrated in Fig. 5. Both ribbons have a width w and their outer edges are separated by d ($d \geq 2w$). As they adhere, they are twisted by an angle $\pi/2$ along an opening of length l. Within the limit $l \gg (w,d)$, the contact length between the ribbons is given by $L - 2l$. For these macroscopic model experiments we assume that the ribbons are not extensible. As a consequence, bringing together the ribbons lifts their middle section by a distance Δz upwards. We write θ for the apparent opening angle at the contact point. Using these geometrical quantities, we now estimate the different energies involved in the assembly process.

3.1 Adhesion

Since the liquid totally wets the surface of the ribbons, separating a pair of adhered ribbons creates two liquid–air interfaces of

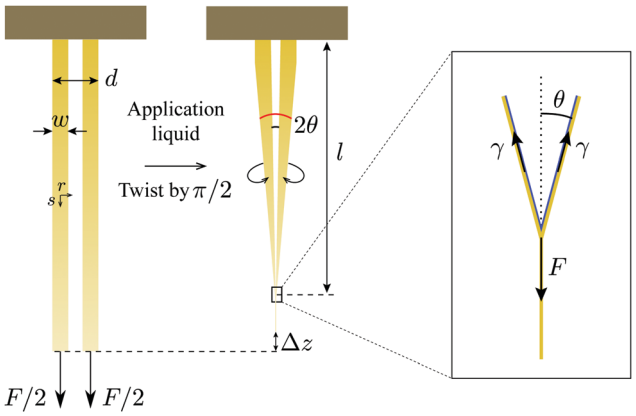

Fig. 5 Parameters for the macroscopic model. L is the total length of the ribbons, w their width and d the distance from one outer edge to the other ($d \geq 2w$). Each ribbon is loaded with an axial force $F/2$ and their adhesion is induced by a wetting liquid of surface tension γ. The opening length l corresponds to the non-sticking part, after assembly. The geometrical definition of the opening angle θ is ambiguous as its value is expected to range between $d/2l$ (red angle line) and $(d - w)/2l$ (black line). In the case of inextensible ribbons, their assembly leads to a vertical displacement by Δz of their middle section. Here, r and s denote the transverse and longitudinal coordinates, respectively.

extension $2l$ (the pair is separated at the top and bottom of the assembly). As a consequence, the cost in surface energy corresponds to

$$U_s = 4\gamma w l \tag{1}$$

where γ is the liquid surface tension.

3.2 Twisting

Twisting a ribbon in an helical mode obviously tend to stretch the edges and compress the center line longitudinally, which results in elastic energy. However, the detailed stress distribution is complex, as shown by Green in his seminal work.[30,31] Counter-intuitive compressive stresses can indeed lead to a variety of buckling patterns, that has been the subject of recent investigations.[25,26] Nevertheless, we consider here the simplest helical mode of a ribbon of length l with a twist angle $\alpha = \pi/2$ and a tension $T = F/2$. Following the classical derivation from Green, the main component of stress is along the longitudinal direction and its non-dimensional form is given by

$$\bar{\sigma}_{ss}(\bar{r}) = \frac{\bar{T}}{2} + \frac{\eta^2}{2}\left(\bar{r}^2 - \frac{1}{12}\right) \tag{2}$$

where $\bar{\sigma} = \sigma/E$, $\bar{T} = F/Etw$, $\eta = \alpha w/l$ and $\bar{r} = r/w$ are the normalized longitudinal stress, applied tension, twist angle and transverse material coordinate, respectively. Note that a transverse component of stress is also present,[26] but its magnitude $\bar{\sigma}_{rr} \sim \eta^2\bar{\sigma}_{ss}$ is negligible in the limit $\eta \ll 1$. The resulting energy is finally given by

$$U = \frac{1}{2}Ewlt\int_{-1/2}^{1/2} \bar{\sigma}_{ss}{}^2(\bar{r})\mathrm{d}\bar{r} \tag{3}$$

Before twisting, the initial elastic energy stored in the ribbon due to the tension equals $Etwl\bar{T}^2/4$. Integrating eqn (3) and subtracting this initial energy thus gives the twist energy (in other words, we integrate the stress without the contribution of $\bar{T}$). Since the system involves 4 pieces of ribbon, we finally obtain

$$U_{tw} = \frac{4}{1440}Etwl\eta^4 = \frac{\pi^4}{5760}\frac{Etw^5}{l^3} \tag{4}$$

with a twist angle $\alpha = \pi/2$.

3.3 Bending

In addition to being twisted, the ribbons are also bent as they approach each other. As a rough estimate, the typical curvature involved is on order of d/l^2, which leads to a bending energy of

$$U_b \sim Et^3w\left(\frac{d}{l^2}\right)^2 l. \tag{5}$$

We thus expect the ratio between the bending and twist energies to scale as

$$U_b/U_{tw} \sim \frac{t^2d^2}{w^4}. \tag{6}$$

Since the width of the ribbons is of the same order of magnitude as their separating distances, the amplitude of the ratio is set by $(t/w)^2$ and is small in the case of thin ribbons. We will thus disregard the effect of bending in our simplified model. From an experimental point of view, the ribbons tend to form a 'Y' shape (Fig. 3), which also suggests that bending may be neglected.

3.4 Tension

The lateral displacement of the ribbons induces a vertical displacement Δz of their middle sections (Fig. 5). Since a load $F/2$ is applied to each ribbon, this displacement corresponds to work $F\Delta z/2$ for each of the 4 pieces of ribbon. We assume that the ribbons are inextensible and that the opening angle is small ($\theta < 0.1$ in our experiments). Using simple geometry, we obtain (Fig. 5)

$$\Delta z = \left(\frac{1}{\cos\theta} - 1\right)l \simeq \frac{\theta^2}{2}l \tag{7}$$

However the definition of θ is subtle as its value *a priori* lays between two bounds $(d - 2w)/2l \leq \theta \leq d/2l$. We define a correction factor β, such as $\theta = \beta d/2l$. Its actual value is expected to lie in the range $1 - 2w/d \leq \beta \leq 1$, and will be determined experimentally. Note that this uncertainty in the opening angle is mainly relevant when the ribbons are very close ($d \backsimeq 2w$). When large separating distances are considered, β indeed tends to unity. The energy corresponding to tension is finally given by

$$U_t = 2F\Delta z = \beta^2\frac{d^2}{4l}F. \tag{8}$$

3.5 Determination of the opening length

The total energy of the system corresponds to the sum of the contributions of the adhesion, twisting and the work of the tensile load:

$$U_{total} = U_s + U_{tw} + U_t = 4\gamma w l + \frac{\pi^4}{5760}\frac{Etw^5}{l^3} + \beta^2\frac{d^2}{4l}F \tag{9}$$

We thus obtain the opening length by minimizing U_{total} with respect to l:

$$4\gamma w - \frac{\pi^4}{1920}\frac{Etw^5}{l^4} - \beta^2\frac{d^2}{4l^2}F = 0 \qquad (10)$$

which can be normalized in the form

$$\frac{\pi^4}{1920}\frac{\bar{w}^4}{\bar{l}^4} + \beta^2\frac{1}{4\bar{l}^2}\bar{T} - \frac{4\gamma}{Et} = 0 \qquad (11)$$

where $\bar{l} = l/d$ and $\bar{w} = w/d$ correspond to the non-dimensional adhesion length and distance, respectively, and $\bar{T} = F/Etw$ to the non-dimensional tension. Elementary algebra leads to the solution (the other solution is negative)

$$\bar{l} = \left[\frac{1}{32}\frac{Et}{\gamma}\left(\beta^2\bar{T} + \sqrt{\beta^4\bar{T}^2 + \frac{\pi^4}{15}\frac{\gamma}{Et}\bar{w}^4}\right)\right]^{1/2} \qquad (12)$$

If we define the characteristic tension $\bar{T}_c = \frac{\pi^2}{\beta^2}\sqrt{\frac{1}{15}\frac{\gamma}{Et}}\left(\frac{w}{d}\right)^2$ the previous expression can be simplified into:

$$\bar{l} = \frac{\pi}{4\sqrt{2}}\frac{w}{d}\left(\frac{1}{15}\frac{Et}{\gamma}\right)^{1/4}\left[\left(\bar{T}/\bar{T}_c + \sqrt{(\bar{T}/\bar{T}_c)^2+1}\right)\right]^{1/2} \qquad (13)$$

Two asymptotic limits are readily defined as the non-dimensional tension is compared $\bar{T}_c$:

$$l/d \simeq \frac{\pi}{4\sqrt{2}}\frac{w}{d}\left(\frac{1}{15}\frac{Et}{\gamma}\right)^{1/4} \quad \text{for} \quad \bar{T} \ll \bar{T}_c,$$

and

$$l/d \simeq \frac{\beta}{4}\left(\frac{Et}{\gamma}\bar{T}\right)^{1/2} \quad \text{for} \quad \bar{T} \gg \bar{T}_c.$$

The first asymptotic regime corresponds to a balance between adhesion and twist. The non-dimensional number Et/γ involved in the expression is also found in different situations where surface tension induces the stretching or compression of elastic membranes[32–34] (here, the ribbon is compressed along the center line and stretched along the edges). Conversely, the second regime corresponds to a balance between adhesion and applied stress. This last situation is similar to a recent study on the capillary adhesion of pre-strained fibers where twist in not involved.[35] In the following Section 4, we aim to determine the value of the parameter β from a comparison with our experiments.

3.6 Variable tension in micro-ribbons

In contrast with our macroscopic experiments, the micro-ribbons are initially submitted to a residual stress $\sigma_{\text{r-SiN}}$ and not to a constant force. This residual stress is due to the LPCVD deposition procedure as described in the experimental Section 2.1. Since their ends are clamped at fixed boundaries, assembling a pair of ribbons tends to stretch them more and induces an additional stress:

$$\sigma_{\text{ind}} = E_{\text{SiN}}\frac{2\Delta z}{L} = \beta^2 E_{\text{SiN}}\frac{d^2}{4lL} \qquad (14)$$

Contrary to the related work with pre-strained fibers,[35] the induced stresses may be of the same order of magnitude as the initial residual stress. As a consequence, both quantities should *a priori* be taken into account in the normalized tension:

$$\bar{T} = \frac{2\sigma_{\text{r-SiN}}}{E_{\text{SiN}}} + \frac{2\sigma_{\text{ind}}}{E_{\text{SiN}}} = \bar{T}_0 + \beta^2\frac{d^2}{2lL} \qquad (15)$$

where $\bar{T}_0 = 2\sigma_{\text{r-SiN}}/E_{\text{SiN}}$ is the normalized initial tension (in our situation $\bar{T}_0 \backsimeq 6.10^{-4}$). With this definition of $\bar{T}$, eqn (11) becomes

$$\frac{\pi^4}{1920}\frac{\bar{w}^4}{\bar{l}^4} + \frac{\beta^2}{4\bar{l}^2}\left(\bar{T}_0 + \frac{\beta^2}{2}\frac{1}{\bar{L}\bar{l}}\right) - \frac{4\gamma}{Et} = 0 \qquad (16)$$

with $\bar{L} = L/d$. This equation does not have any direct analytical solution but can readily be solved numerically.

4 Results and discussion

4.1 Determination of the correcting factor β *via* macro experiments

We propose to use our experimental data to infer the value of the correcting factor β. This factor may, in principle, depend on the ratio w/d but is expected to tend towards unity in the limit $w \ll d$. The experiments presented in Section 2.2.2 correspond to the most discriminating configuration $d = 2w$ (additional data with $d = 3w$ and $d = 4w$ are presented as ESI† in Fig. S2). We represent in Fig. 6 the non-dimensional opening length $\bar{l} = l/d$ as a function of the normalized force $\bar{T} = F/Etw$. All the data collapse to a single master curve which is compared with the theoretical prediction from eqn (12) for different values of β. We observe that $\beta = 1$ corresponds to the best fit, and we will therefore select this value for our further predictions. In our experiments, the order of magnitude of the characteristic normalized tension is $\bar{T}_c \sim 4.10^{-4}$. For higher and lower tensions

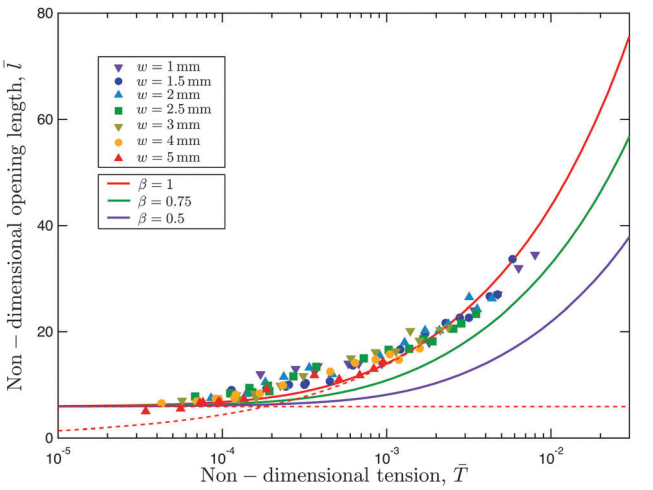

Fig. 6 Normalized opening length $\bar{l} = l/d$ as a function of the normalized tension $\bar{T} = F/Ehw$ for the same experimental data plotted in Fig. 4 ($\bar{w} = w/d = 1/2$). The lines correspond to eqn (12) at different values of the correction factor β: 1, 0.75 and 0.5, respectively. The dashed lines show the asymptotic limits $T \ll T_c$ and $T \gg T_c$.

the data follows the respective asymptotic limits described in Section 3.5. Nevertheless we observe some deviation of the experimental data from the theoretical curve for $\bar{T} \gtrsim 10^{-3}$. We interpret this discrepancy as due to the formation of creases along the ribbon (see Fig. S3 in the ESI†). Indeed, intriguing studies have recently evidenced different buckling instabilities occurring with twisted ribbons[25,26] and the peculiar mechanical properties of localized folds.[36] As demonstrated in these studies the smooth helicoidal configuration is only valid for low values of the normalized angle $\pi w/l$ and relatively large tension (typically, $\pi w/l \lesssim 0.3$ and $\bar{T} \gtrsim 4.10^{-3}$) which is consistent with our observations.

As a partial conclusion, model macroscopic experiments are fairly well described by our simplified theoretical model with $\beta = 1$. In other words, the relevant distance separating the ribbons is d. In the following section, we propose to extend this model to the case of microscopic ribbons obtained by micro-fabrication techniques.

4.2 Microscopic scale experiments

We conducted different sets of experiments with ribbons of thickness t = 107 nm and t = 270 nm. Different widths, separating distances and total lengths were probed, in the range 5 μm $\leq w \leq$ 20 μm, 15 μm $\leq d \leq$ 45 μm and 100 μm $\leq L \leq$ 1 mm, respectively. The corresponding opening lengths are plotted in Fig. 7a as a function of the total stress acting on the ribbons $\sigma_{\text{r-SiN}} + \sigma_{\text{ind}}$, with $\sigma_{\text{r-SiN}}$ = (169 ± 25) MPa and σ_{ind} as estimated from eqn (14). Each data point corresponds to an average of measurements on 5 identical sets of structures present on the same wafer. The induced stress is in the range 85 MPa to 198 MPa for t = 270 nm while it is higher for thinner ribbons with σ_{ind} from 158 MPa to 568 MPa. Indeed, stiffer samples are less prone to be deformed under the action of capillary forces. As a general result, we observe that the opening length l increases with w (yellow data points higher than the red ones) and d (darker data points higher than the light ones). Conversely, l decreases slightly when longer ribbons are considered (larger points lower than the smaller ones). The same data are represented in Fig. 7b in their normalized version and compared to the solution of eqn (16) (with γ = 72 mN m^{-1}). Since each dataset (same t) corresponds to a certain range of non-dimensional distance $\bar{d}$, the theoretical solutions are represented by lines for each particular range (t = 107 nm in red and t = 270 nm in blue). The agreement between the model and the experiments is fairly good. This result is confirmed by the analysis of the dependence of the opening length on the individual different parameters (Fig. 8). In the worst case, the difference between the calculated and the measured value of l is indeed less than 30%.

In our estimates, we used the surface tension of water as capillary forces from water bridges drives the adhesion of the ribbons. However, unlike the case of the non-volatile silicone oil used for macroscopic experiments, water eventually evaporates and we may expect the micro-ribbons to reopen. Nevertheless van der Waals interactions[37] or more generally adhesion forces due to a molecular layer of water or to the presence of debris

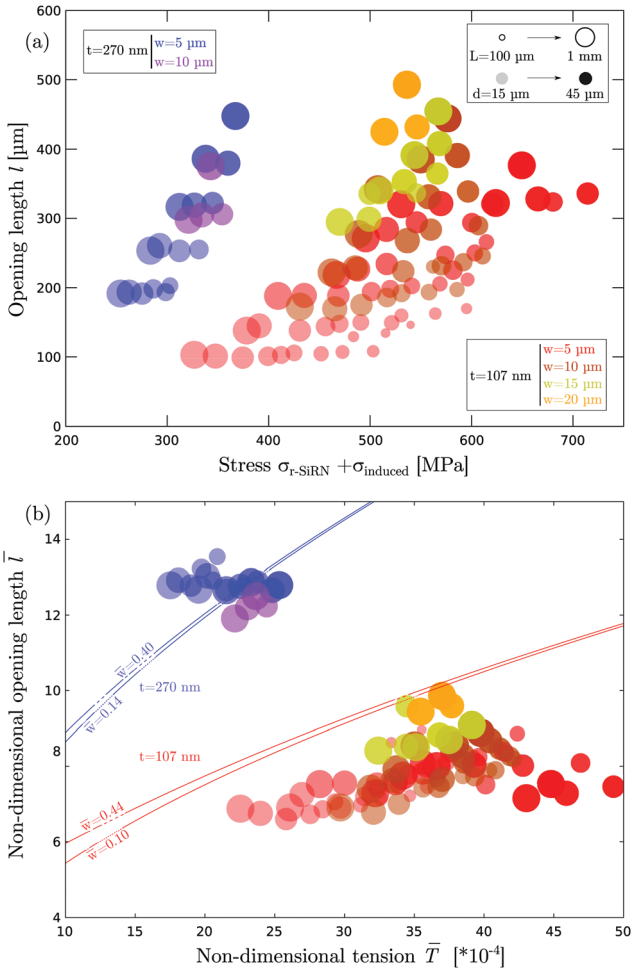

Fig. 7 Opening length as a function of the stress acting on the ribbons in the case of SiN micro-structures. The total stress is estimated using eqn (14). The experiments are divided into two groups corresponding to t = 107 nm and t = 270 nm, respectively. For each group, the different widths are identified by the colour of the symbols, the separating distances by the colour intensity, and the total lengths of the ribbons by the size of the symbols. (a) Raw data. (b) Normalized representation of the same data where the normalized tension $\bar{T}$ is deduced from eqn (15). For a given group of the same thickness, the data correspond to different values of non-dimensional width $\bar{w}$. We represent by lines the theoretical solution from eqn (16) for the the bounds of the corresponding range in $\bar{w}$.

resulting from the etching procedure can maintain the beams in contact.[8,9,38] In principle, the liquid surface tension γ should therefore be replaced by the adhesion energy $\gamma_{\text{adh}}/2$ in our derivations (the factor 1/2 accounts for the two liquid–air interfaces created as the surfaces are separated). Although their magnitude is of the same order as the surface tension, such stiction forces are famously difficult to measure precisely. As the range of action of these interactions is short[39] (typically less than 100 nm), stiction usually relies on capillary bridges to bring the adhered elements in close contact.[14] We present in Fig. S1 from ESI† a close-up view of the adhering region before and after evaporation in a macroscopic experiment conducted with ribbons in silicone rubber bridged with a volatile liquid (ethanol). The ribbons remain in contact after the evaporation

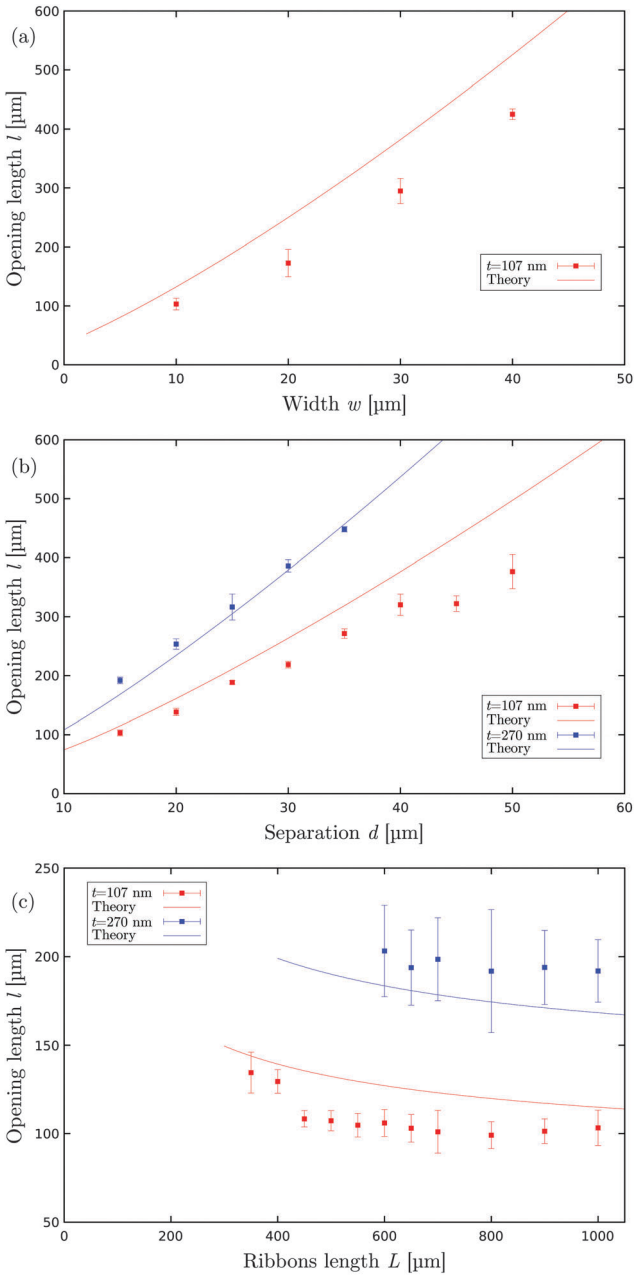

Fig. 8 Opening at the extremities as a function of the individual geometrical parameters for samples of thickness t = 107 nm and t = 270 nm, respectively. Each points is an average of measurements on SEM pictures from 5 identical set of structures present on the same wafer. One wafer was used for each thickness t. Theoretical lines are obtained using eqn (16) with γ = 72 mN m^{-1}. (a) Dependence on the width for a constant gap between the ribbons of 5 µm (therefore $d = 2w + 5$ µm) and a length L = 1000 µm. (b) Dependence on the separation distance for L = 1000 µm and w = 5 µm. (c) Dependence on the total length for w = 5 µm and d = 15 µm.

and the change in opening length is barely visible (in this particular case using soft ribbons promotes adhesion through van der Waals interactions even at macroscopic scales). This observation is confirmed by the Movie 1 in the ESI.† At the end of the video a pair of ribbons is observed while the water evaporates and the contact line stays still after complete evaporation. Our model should only predict a minimum opening length and further work would be necessary to fully understand the solid bridging in our assembly, which is beyond the scope of the present study. Nevertheless, the fair agreement between the calculated and measured opening lengths suggests that using the surface tension of water provides a good estimate of the adhesion energy.

4.3 Non-twisting configurations

All experiments involving separate pairs of ribbons have led to a twisting self-assembly (or did not assemble at all). However, other configurations were observed in experiments conducted with multiplets. We present in Fig. 9 two examples of sextuplets treated through the same rinsing and drying procedure we have described. Although the geometrical parameters are in the same range as those of the previous experiments (t = 107 nm, w = 20 µm, $d \sim 50$ µm, L = 1 mm), we obtain different types of assemblies. For instance, a pair of ribbons gathered side by side along their thickness, while three pairs partially overlapped without twisting. Nevertheless a pair followed the regular twisting mechanism. Such observations are not limited to microscopic scale experiments and similar states are also observed in macroscopic experiments (they can be forced with a syringe tip).

These configurations are surprising as they involve a flexion of the beam across its width and a corresponding bending

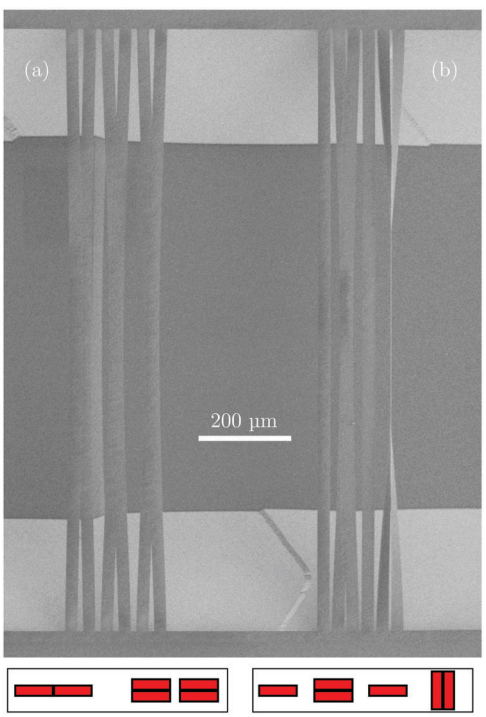

Fig. 9 Assembly of sextuplets following the same procedure employed for the previous experiments. The geometrical parameters are in the same range of the previous experiments conducted with separated pairs: t = 107 nm, w = 20 µm, L = 1 mm and a gap of 10 µm for sextuplet (a) and 5 µm for sextuplet (b). Although one pair follows the regular twisting self-assembly, we obtain different configurations for the other ribbons. One pair of ribbons gathered side by side along their thickness, while three pairs partially overlapped without twisting.

stiffness on the order of $Ew^3t/12$. As a first approximation, the curvature induced in each beam is given by $w/2l^2$. Since four portions of the beams are bent, a crude estimate of the bending energy is

$$U_b \sim 4\frac{Ew^3t}{12}\left(\frac{w}{2l^2}\right)^2 l \sim \frac{1}{12}\frac{Etw^5}{l^3}, \quad (17)$$

which is significantly larger than the twisting energy U_{tw} we have estimated in Section 3.2 (for the same value of l). We expect the stretching energy to follow the same scaling law as in the case of twisted ribbons. Finally, the adhesion energy is similar when the ribbons overlap and decreases by a factor t/w if they adhere side by side. Although more careful estimates of the different energies would be necessary for a definitive conclusion, these multistable configurations should be less favorable than the twisting ones (especially in the case $d \gg 2w$ when the determination of the bending and stretching energies are less ambiguous). The appearance of such configurations probably results from the dynamics of the assembly. In the case of separate pairs, a single capillary bridge connects the inner edges of the ribbons. However, we expect both edges of the inner ribbons of a multiplet to be in contact with menisci during their assembly. A detailed study of the such dynamics is nevertheless beyond the scope of the current study and we hope that these preliminary results will motivate further investigations.

5 Conclusions

We have described a mode of capillary induced assembly of parallel micro-ribbons clamped at both sides, involving a rotation of their central part by an angle of 90°. We developed a simplified theoretical description of this self-assembly based on macroscopic model experiments. The main physical ingredients rely on a balance between the surface tension and the addition of twisting and stretching energies of the ribbon (the bending energy appears to be negligible). As a general trend, the adhesion length ($L - 2l$) decreases as the distance between the ribbons is augmented or when wider or thicker specimen are considered. Conversely this adhesion length is larger for longer ribbons. These variations are in quantitative agreement with our model. To the best of our knowledge, this twisting configuration is original. We hope that this study will pave the way for novel solutions to design three-dimensional structures which cannot be fabricated through standard lithography techniques. More intricate structures such as a 'bicycle wheel' or ribbons with flaps on their side are for instance presented in Fig. S4 and S5 in the ESI.† Further work will nevertheless be necessary to capture the different multistable configurations such systems may present.

Acknowledgements

We thank Benoît Roman for stimulating discussions as well as R. G. P. Sanders for his help with measurements and K. Ma for his precious help in the cleanroom. This work would have never been possible without the inspiring research from our regretted colleague J. W. Honschoten. This work was partially funded by the Dutch Technology Foundation STW, applied science division of NWO, the technology program of the Ministry of Economic Affairs, and by the Interuniversity Attraction Poles Programme (IAP 7/38 MicroMAST) initiated by the Belgian Science Policy Office and the National Science Foundation under Grant No. NSF PHY11-25915.

References

1 A. Boisen, S. Dohn, S. S. Keller, S. Schmid and M. Tenje, *Rep. Prog. Phys.*, 2011, **74**, 036101.
2 M. J. Madou, *Fundamentals of Microfabrication*, CRC Press, New York, 1997.
3 M. Boncheva and G. M. Whitesides, *MRS Bull.*, 2005, **30**, 736–742.
4 M. Mastrangeli, S. Abbasi, C. Varel, C. Van Hoof, J.-P. Celis and K. F. Boehringer, *J. Micromech. Microeng.*, 2009, **19**, 083001.
5 T. G. Leong, A. M. Zarafshar and D. H. Gracias, *Small*, 2010, **6**, 792–806.
6 M. Mastrangeli, *Adv. Mater.*, 2015, **27**, 4254–4272.
7 B. Roman and J. Bico, *J. Phys.: Condens. Matter*, 2010, **22**, 493101.
8 N. Tas, T. Sonnenberg, H. Jansen, R. Legtenberg and M. Elwenspoek, *J. Micromech. Microeng.*, 1996, **6**, 385–397.
9 C. Mastrangelo, *Tribol. Lett.*, 1997, **3**, 223–238.
10 C. Hui, A. Jagota, Y. Lin and E. Kramer, *Langmuir*, 2002, **18**, 1394–1407.
11 N. Tas, M. Escalante, J. van Honschoten, H. Jansen and M. Elwenspoek, *Langmuir*, 2010, **26**, 1473–1476.
12 D. Chandra and S. Yang, *Acc. Chem. Res.*, 2010, **43**, 1080–1091.
13 M. De Volder and A. J. Hart, *Angew. Chem., Int. Ed.*, 2013, **52**, 2412–2425.
14 S. Tawfick, J. Bico and S. Barcelo, *MRS Bull.*, 2016, **41**, 108–114.
15 D. Gracias, V. Kavthekar, J. Love, K. Paul and G. Whitesides, *Adv. Mater.*, 2002, **14**, 235–238.
16 J.-H. Cho, A. Azam and D. H. Gracias, *Langmuir*, 2010, **26**, 16534–16539.
17 J. W. van Honschoten, T. Berenschot, J. W. Ondarçuhu, R. G. P. Sanders, J. Sundaram, M. Elwenspoek and N. R. Tas, *Appl. Phys. Lett.*, 2010, **97**, 0141031.
18 J. van Honschoten, A. Legrain, J. Berenschot, L. Abelmann and N. Tas, Micro Electro Mechanical Systems (MEMS), 2011 IEEE 24th International Conference on 2011, pp. 288–291.
19 A. Legrain, T. G. Janson, J. W. Berenschot, L. Abelmann and N. R. Tas, *J. Appl. Phys.*, 2014, **115**, 214905.
20 A. Legrain, E. J. W. Berenschot, N. R. Tas and L. Abelmann, *PLoS One*, 2015, **10**, e0125891.
21 A. Legrain, J. Berenschot, N. Tas and L. Abelmann, *Microelectron. Eng.*, 2015, **140**, 60–66.
22 B. Pokroy, S. H. Kang, L. Mahadevan and J. Aizenberg, *Science*, 2009, **323**, 237–240.
23 S. H. Kang, B. Pokroy, L. Mahadevan and J. Aizenberg, *ACS Nano*, 2010, **4**, 6323–6331.
24 A. Grinthal, S. Kang, A. Epstein, M. Aizenberg, M. Khan and J. Aizenberg, *Nano Today*, 2012, **7**, 35–52.

25 J. Chopin and A. Kudrolli, *Phys. Rev. Lett.*, 2013, **111**, 174302.
26 J. Chopin, V. Démery and B. Davidovitch, *Journal of Elasticity*, 2014, **119**, 137–189.
27 G. Stoney, *Proc. R. Soc. London, Ser. A*, 1909, **82**, 172–175.
28 P. Temple-Boyer, C. Rossi, E. Saint-Etienne and E. Scheid, *J. Vac. Sci. Technol., A*, 1998, **16**, 2003–2007.
29 O. Tabata, K. Kawahata, S. Sugiyama and I. Igarashi, *Sens. Actuators*, 1989, **20**, 135–141.
30 A. E. Green, *Proc. R. Soc. London, Ser. A*, 1936, **154**, 430–455.
31 A. E. Green, *Proc. R. Soc. London, Ser. A*, 1937, **161**, 197–220.
32 J. Huang, M. Juszkiewicz, W. de Jeu, E. Cerda, T. Emrick, N. Menon and T. Russell, *Science*, 2007, **317**, 650–653.
33 J. Chopin, D. Vella and A. Boudaoud, *Proc. R. Soc. A*, 2008, **464**, 2887–2906.
34 J. Hure, B. Roman and J. Bico, *Phys. Rev. Lett.*, 2011, **106**, 174301.
35 C. Duprat and S. Protière, *EPL*, 2015, **111**, 56006.
36 J. Chopin and A. Kudrolli, *Soft Matter*, 2016, **12**, 4457–4462.
37 F. Delrio, M. De Boer, J. Knapp, E. Reedy, P. Clews and M. Dunn, *Nat. Mater.*, 2005, **4**, 629–634.
38 R. L. Alley, G. J. Cuan, R. Howe and K. Komvopoulos, Solid-State Sensor and Actuator Workshop, 1992. 5th Technical Digest., IEEE, 1992, pp. 202–207.
39 J. N. Israelachvili, *Intermolecular and surface forces: revised third edition*, Academic press, 2011.

